PROFESSOR MARAT KHAFIZOV (Orcid ID : 0000-0001-8171-3528)

Article type : Article

Impact of irradiation induced dislocation loops on thermal conductivity in ceramics

Marat Khafizov,[a*] Janne Pakarinen,[b,c] Lingfeng He,[c,d] David H. Hurley[d]

[a] Mechanical and Aerospace Engineering, The Ohio State University, Columbus, OH, 43210

[b] Belgian Nuclear Research centre (SCK•CEN), Boeretang 200, B-2400, Mol, Belgium

[c] Department of Engineering Physics, University of Wisconsin, Madison, WI, 53706

[d] Idaho National Laboratory, Idaho Falls, ID, 83415

Abstract

Experimental work aimed at understanding the role of dislocation loops in limiting phonon mediated thermal transport in ceramics is presented. Faulted dislocation loops, having diameters of a few nanometers, were introduced by irradiating a polycrystalline cerium dioxide sample with 1.6 MeV protons at 700°C. XRD analysis indicated that irradiated samples retained their crystalline structure and exhibit very little lattice expansion suggesting a low concentration of point defects. Further microstructure characterization using transmission electron microscopy revealed that interstitial type faulted dislocation loops were primarily created as expected for these irradiation conditions. Thermal conductivity of the damaged layer was measured using a

modulated thermoreflectance approach. Analysis of the experimental data using the classical Klemens-Callaway approach reveals that the conductivity reduction is primarily due to dislocation loops, while point defects and voids play only a minor role. These results provide experimental confirmation that faulted loops offer a unique arrangement for displaced atoms that leads to an unusually large reduction of thermal conductivity.

Keywords: radiation damage, thermal conductivity, dislocation loops

* Corresponding author: khafizov.1@osu.edu

Introduction

The impact of nanoscale microstructural features on thermal transport in ceramic materials has implications for an array of energy applications.(1-4) For nuclear applications, while the nanoscale features provide radiation tolerance in ceramics(5-7), they may have a detrimental impact on the ability of the material to transport heat. This could limit use of materials with nanoscale features in components with a strict thermal management requirement. The objective of this work is to evaluate how thermal transport is influenced by faulted dislocation loops, microstructure features that are developed in crystalline materials caused by displacement damage and are critical to the radiation tolerance of ceramics against swelling.

Under irradiation, dislocation loops are formed when displaced atoms cluster into extended defects.(8) Interstitial dislocation loops can be visualized as a disk shaped extra plane of atoms having diameters ranging from a few nanometers to a few tens of nanometers. These two-dimensional (2D) features aligned along a particular crystallographic orientation that introduce a fault in the stacking sequence of the atomic planes (faulted loops). In this work, we consider (111)-oriented loops in a fluorite crystalline structure known as interstitial Frank loops that introduce a fault in the ABC-stacking of a face-centered cubic structure. Another class of 2D structures supported in fluorites are perfect loops aligned along (110) planes and unlike (111)-loops they do not introduce a fault in the stacking sequence.(9) Radiation resistance of ceramic materials is generally attributed to a behavior where the faulted loops form a stable structure with no subsequent transformation into perfect loops. This configuration offers conditions favorable

for newly displaced atoms to be absorbed by a vacancy rather than cluster into existing loops. (10, 11)

The potential impact of dislocation loops on thermal conductivity has been previously considered as part of multiple effects studies.(12) These studies considered samples irradiated inside research test reactors with the objective to understand the combined impact of multiple types of defects on thermal conductivity. (13-15) Independently, a number of modeling efforts have been dedicated to the investigation of the impact of radiation induced defects on thermal transport.(16-18) Experimental efforts addressing single effects have been limited to point defect studies that considered non-stoichiometric and alloyed oxides, as well as the impact of impurities.(19-22) Unlike previous studies, the goal of the current study is to isolate the impact of dislocation loops on thermal conductivity. This is achieved through tailored irradiation of cerium dioxide (CeO_2) using energetic protons derived from an ion beam accelerator.

Ion beam irradiation has been extensively utilized as a convenient tool to understand the fundamental mechanisms of irradiation damage evolution as a surrogate for displacement damage caused by energetic neutrons and/or product of nuclear reactions.(23) It offers an attractive method for single effect studies important for the development of predictive models that relate damage to physical properties of materials such as thermal conductivity.(17, 24) However, for thermal transport studies aiming to isolate the impact of dislocation loops, utilizing ion irradiation pose two important experimental challenges.

First, the damage layer is extremely thin, extending only a few microns below the surface, not allowing conventional laser flash measurements to be implemented. Investigations of thermal transport in ion beam irradiated samples has been recently demonstrated with the introduction of laser-based approaches that provide the necessary depth resolution.(25-28) Laser-based modulated thermoreflectance techniques have been shown to provide the spatial resolution needed to isolate thermal properties of this thin damage layer from that of the bulk. Recently, time domain thermoreflectance was used to study the influence of inert gas ion irradiation on thermal transport in UO_2 and SiC.(29, 30) This approach which has unparalleled resolution in the depth direction is well suited to measure changes in conductivity due to ion irradiation whose damage profile is limited to few hundreds of a nanometer.(25) Complementing the time domain approach, laterally resolved modulated thermoreflectance microscopy has been used to measure

conductivity degradation due to krypton irradiation in carbides and proton irradiation in silicon with damage profiles extending beyond a few micrometers.(31, 32)

The second challenge involves relating the fundamental physical mechanisms that limit thermal transport to specific microstructural features. Ion irradiation typically produces a complex change to the microstructure that includes point defects, defect clusters having a range of size distributions, dislocation loops and voids.(33-36) Point defects are strong phonon scattering centers that usually screen out the influence of other extended defects. This makes it difficult to study the influence of extended defects on thermal transport.

Here, we present experimental work aimed at isolating the influence of irradiation induced dislocation loops on thermal conductivity. The work consists of a careful selection of irradiation conditions to introduce a dislocation loop dominant microstructure suitable for measurement using a modulated thermoreflectance (MTR) method. Modulation frequencies in the 10 – 100 kHz range were used and the corresponding thermal diffusion lengths are well suited to investigate the relatively thick damage plateau region.(25, 37) Additionally, our irradiation conditions were chosen to achieve a high mobility of point defects, so that their concentration is minimized through either recombination or clustering into extended defects.(5, 38) A classical model for phonon mediated thermal transport impacted by various lattice defects was employed to analyze the experimental results. In the remainder of this article, sample fabrication, microstructure characterization, thermal conductivity measurements, and a discussion of the prominent phonon scattering mechanism are presented.

Experimental Methods

Two ceria samples sliced from commercially available sintered pellets (AlfaAesar) have been irradiated at T = 700°C using 1.6 MeV protons derived from a NEC Pelletron Tandem accelerator to a fluence of 2.8×10^{18} and 1.4×10^{19} ions/cm^2.(39, 40) 700°C corresponds to a temperature at which point defects are sufficiently mobile and are expected to cluster into extended defects as was shown in previous annealing and microstructure characterization studies of irradiated CeO_2.(33, 41) SRIM software calculations were performed in "ion distribution and quick damage mode" according to the procedure given in Stoller et al.(42) Displacement energies of 20 and 40 eV were used for O and Ce. In the plateau region confined to the top 16

μm, the higher fluence produced a damage of ~ 1.0 dpa and the lower fluence led to damage of ~ 0.2 dpa. The plateau region is followed by 2 μm thick layer having significantly higher damage than the plateau region. It is assumed that the microstructure is homogeneous across the plateau region and its thickness is suitable for thermal transport measurements.(37)

Irradiation damage was characterized using transmission electron microscopy (TEM). The TEM lamellae were created by coarse trenching 20 μm × 15 μm ×1 μm samples using a focused ion beam (FIB) system. A platinum coating was deposited to protect the surface before trenching. Samples were thinned in the FIB down to a final milling step of 5 kV at 77 pA ion emission current until small perforations were observed. FIB damage was cleaned with a final polish using 2 kV at 27 pA ion emission current. Scanning transmission electron microscopy (STEM) was employed to measure the dislocation loop size and density. Electron energy loss spectroscopy (EELS) was used to determine the FIB lamina thickness. STEM and EELS were conducted on a FEI Titan (S)TEM with CEOS probe aberration corrector operated at 200 kV. Irradiation damage was also characterized using X-ray diffraction (XRD). A Siemens Stoe X-ray diffractometer using Cu K_α radiation (40 kV, 2.5 mA) was employed in omega-2theta geometry.

Thermal conductivity was measured using a modulated thermoreflectance (MTR) technique described in detail previously.(43, 44) Prior to thermal characterization, samples and a reference glass slide were coated with a 50 nm thick aluminum layer using thermal evaporation, whose thickness was verified using picoseconds acoustics. An amplitude modulated pump was used as a heating source which excites a thermal wave inside the sample. A second probe beam was used to measure the resulting thermal wave profile by scanning over the excitation region and measuring its temperature induced reflectivity change.(25) Thermal wave profiles were analyzed using a continuum based heat diffusion model to extract the thermal conductivity of the irradiated ceria layer.(37) In this analysis, specific heat and density of the aluminum film and ceria are considered to be known. Thermal conductivity of metal transducer was measured using a reference glass substrate with known thermal properties.(44) It is also assumed that the specific heat of the irradiated region is unchanged. To avoid multiparameter fitting, measured thermal wave profiles were analyzed using a two-layer model: a thin metal film on a substrate, where the substrate represents the plateau region. (4) Analysis were performed over a 10-100 kHz frequency range where the thermal penetration depths is such that the peak damage layer

and unirradiated region have minimal influence on the measured thermal wave profiles and sufficiently deep to provide optimal sensitivity to the plateau damage region. (32, 37)

Results

Figure 1 shows representative STEM micrographs which clearly reveal the presence of irradiation induced dislocation loops in both samples. As expected, the high irradiation dose sample contains larger loops and higher loop density. The dislocation loop average radius R_d and volume density n_d were determined by analyzing a series of STEM micrographs and are listed in Table I. Each reported value is an average of 5 measured areas for the number density measurements and of 50-200 measured features for the size measurements. The loop size was determined by the length of the longer axis of the elliptical shaped feature. The evolution of the loop diameter follows a previously reported trend in $R_d \propto F^{0.33}$, where F represents ion dose, and attributed to growth mechanism governed by interstitial mobility.(45)

Analysis for the nature of the loop was performed in TEM mode. Two families of edge-on loops were imaged with the electron beam close to the [011] beam axis. High-resolution TEM images (Fig. 2a) accompanied by Fourier transforms in Figs. 2(b) and 2(c) clearly show that the loops lie on the $(1\bar{1}1)$ and $(\bar{1}\,\bar{1}1)$ planes and are likely **b** = 1/3(111) type stacking fault loops in agreement with previous TEM results of electron(46) and ion irradiated ceria.(47) These loops are generally seen in the early stages of irradiation damage and are confirmed by molecular dynamics simulations.(48) No microstructure features that could be identified as irradiation induced voids were observed in these samples.

XRD analysis confirms that irradiated samples remained crystalline with a very small lattice expansion as shown in Fig. 3. Lattice expansion was estimated and listed in Table I. The higher dose 1.0 dpa sample exhibits a larger lattice expansion than 0.2 dpa sample as expected.

Early work on fluorite crystals have shown that point defects, most notably vacancy-interstitial Frenkel pairs, induce considerable lattice swelling in materials irradiated at low temperatures.(41, 49) The high temperature irradiation samples investigated in this paper exhibit

an order of magnitude smaller expansion $\Delta a/a = 4.1 \times 10^{-4}$ than previously reported $\Delta a/a \approx 5 \times 10^{-3}$ for low temperature ion irradiated CeO_2 and uranium dioxide (UO_2) despite a higher dose.(40, 41, 50) This is attributed to enhanced mobility of point defects at high temperatures and the tendency of point defects to cluster into extended defects.(34, 38) Specifically, in this work, dislocation loops appear to be a predominant form for defect clusters as revealed by TEM analysis presented above. The XRD suggest that a very small concentration of point defects remains in the lattice after irradiation. These result are consistent with the annealing studies of irradiated CeO_2, where a complete recovery of lattice expansion is reported in room temperature ion irradiated samples when the annealing temperature reaches 700°C.(41)

The effect of dislocation loops on the lattice swelling observed by XRD has been a subject of debate. A general conclusion from the early work implies that the small (point-defect scale) loops have an effect on the lattice constant as measured by XRD while the effects become smaller as the loops grow larger.(51) The upper limit on lattice expansion caused by dislocation loops can be estimated using $\Delta a/a = 1/3\,\pi b R_d^2 n_d$, where b is the Burgers vector of the dislocation loop.(52) Table I summarizes the results of lattice expansion analysis. It is evident that dislocation loops alone are unable to account for observed lattice expansion. This suggests that there are additional defects, other than loops that contribute to lattice expansion.(41)

Irradiations at high temperature and low oxygen partial pressure produce an environment under which CeO_2 undergoes chemical reduction that introduces oxygen vacancies.(53) Previous reports on ion irradiation of CeO_2 have reported on this behavior, which was accompanied by notable lattice expansion.(54, 55) Considering 700 °C irradiation, most of the irradiation induced point defect should in principle be recovered as experimentally suggested and implied by high mobility of the point defect. We speculate that the primary contribution for additional lattice expansion is from oxygen vacancies caused by the reducing environment present inside the ion irradiation chamber.

Another irradiation induced defect known to impact thermal transport are voids.(18) While the majority of vacancies created under displacement damage recombine with interstitials, a very

small fraction of them is expected to cluster into voids.(33) Even though our TEM observations do not provide any conclusive evidence for void nucleation, their potential impact is still included in our thermal transport analysis. In summary, our microstructure characterization reveals extended defects in the form of interstitial type dislocation loops and we speculate that there are some point defects or defect clusters, whose exact structure cannot be readily identified using TEM.

The phase of the thermal wave profiles measured at modulation frequency f = 10 kHz using MTR are plotted in Fig. 4(a). The phase profile exhibits a characteristic linear dependence proportional to materials' thermal properties.(37) Effective diffusivity versus modulation frequency determined by appropriately normalizing the slopes extracted from the linear sections of the profiles measured over 10- 100 kHz frequency range are plotted in Fig. 4(b).(56) Steeper profile with larger slope and smaller effective diffusivity is a direct indication of thermal conductivity reduction in irradiated samples.(32) Quantitative determination of conductivity in the plateau region that accounts for transducer layer and considers only profiles that have minimal sensitivity to peak damage and undamaged section of the samples follows a procedure outlined in Riyad et al.(37)

Table I lists the measured conductivities for both irradiated samples and compares them to the as-received sample. The reduction of conductivity in both irradiated samples is notable, with a larger reduction in the high dose sample, as expected. Qualitatively, there is a common trend that higher dose sample has a larger conductivity reduction, a larger diameter and concentration of the loops, and exhibits more lattice swelling. Considering the percentage in conductivity reduction and comparing it to lattice swelling and dislocation loop evolution (Table I), we observe a stronger correlation between conductivity reduction and dislocation loop size and density. This quick observation suggests that, as desired, the conductivity reduction in the irradiated samples is influenced primarily by phonon scattering at dislocation loops. Further analysis of the experimental results is performed using a thermal transport model that considers the influence of dislocation loops, voids and irradiation induced point defects.(4, 14, 57)

Discussion

A standard model describing phonon mediated thermal transport in crystalline systems was used to analyze the thermal conductivity results. According to the Klemens-Callaway approach, thermal conductivity is given by:(58, 59)

$$\kappa = \int_0^{\omega_D} \frac{C(\omega,T)v_s^2}{\tau^{-1}(\omega)} \frac{\omega^2 \mathrm{d}\omega}{2\pi^2 v_s^3}, \quad (1)$$

where $C(\omega,T) = k_B x^2 e^x/(1-e^x)^2$, $x = \hbar\omega/k_B T$, ω - phonon frequency, T - temperature, $\hbar$ - Plank's constant, k_B - Boltzmann constant, v - sound velocity, and ω_D - Debye phonon frequency. Phonon scattering rate $\tau^{-1}(\omega)$ is a combination of the following phonon scattering processes: intrinsic 3-phonon processes, impurities in the as-received sample, and irradiation induced point defects, dislocation loops, and voids added using Mattiesen rule.(56, 59) For the intrinsic 3-phonon and impurity scattering we use the relations $\tau_{3ph}^{-1}(T,\omega) = BT\omega^2 \exp(-T_D/3T)$ and $\tau_{imp}^{-1}(\omega) = A_0\omega^4$, respectively where use B = 1.6× 10^{-18}s/K, ω_D = 5.4× 10^{13} Hz, T_D = 409 K, v_s = 3270 m/s and A_0 = 44.1 × 10^{-44}s^3 obtained in previous work on unirradiated CeO_2.(4) Parameters ω_D and T_D are calculated based on the Debye model using a sound velocity v_s averaged over one longitudinal and two transverse acoustic modes based on bulk properties of CeO_2.(4, 60) The impact of irradiation damage on these parameters is negligible compared to the impact on phonon scattering rates. The impact of irradiation damage on phonon scattering rates for individual defect types is described next.

Irradiation induced point defects are accounted for using

$$\tau_{pd}^{-1}(\omega) = \frac{V_0}{4\pi N v_s^3}\Gamma\omega^4 \quad (2)$$

where Γ is the point defect scattering parameter, which is proportional to the defect concentration. (59) Here point defects are either isolated vacancies, interstitials or small defect clusters. Larger voids, acting like 3D objects, scatter phonons according to

$$\tau_v^{-1}(\omega) = \pi v_s r_v^2 n_v \quad (3)$$

where r_v and n_v are the average radius and concentration of voids.(61)

Treatment of dislocation loops requires closer attention because the literature on analytical expressions for dislocation loops is very limited.(62) Three approaches were considered, two are based on work by Klemens and one based on an expansion of this work.(59, 62) The first approach treats the circumference of the loop as a dislocation line, the second assumes a platelet, and third considers the internal feature of the loop as a stacking fault. The dislocation line model, which only includes the contribution from the extended strain field, is given by (59)

$$\tau_{line}^{-1}(\omega) = 0.06\gamma^2 b^2 N_d \omega, \quad (4)$$

where γ - Gruneisen parameter, b - dislocation line Burgers vector, and N_d - dislocation line density, defined as the number of lines per unit area, $N_d = 2\pi R_d n_d$. Here we use γ = 2.05 obtained from atomistic calculation of thermal conductivity in CeO_2.(63) While the scattering from platelet inclusion is (14):

$$\tau_{plate}^{-1}(\omega) = \frac{24\pi b^2 R_d^2 n_d}{v_s}\omega^2. \quad (5)$$

Lastly, the scattering by stacking faults is given by (59):

$$\tau_{fault}^{-1}(\omega) = \frac{0.7a^2\gamma^2 N_s}{v_s}\omega^2, \quad (6)$$

where a is the lattice constant and N_s is number of stacking faults per unit length, $N_s = \pi R_d^2 n_d$.

Since there is some certainty about density and size of the dislocation loops, their influence on thermal transport is considered first. The initial step is to compare the predictions of 3 models for dislocation loops. The predictions are shown in Fig. 5(a), where the relative reduction in conductivity versus dose is plotted for experimental and model values. The dislocation line model (Eq. 4, black dotted line) suggests only a negligible reduction in conductivity, which indicates it is not a suitable model for the description of faulted loops. This doesn't come as a surprise, since atomic level calculations have previously identified a systematic underestimate provided by Eq.4 to capture the impact of dislocations.(16, 64) A platelet model defined by Eq. 5 (green dash-dot line), initially used for dislocation loops overestimates the reduction. The stacking fault model (Eq.6 and red line), on the other hand, provides an estimate that is in remarkable agreement with the experimental values with no fitting parameters. It is important to note that the stacking fault and platelet inclusion models share the same ω^2 functional form. These models only differ in the way phonon anharmonicity is accounted for, resulting in different prefactors.

Next, we consider the influence of voids, which are potentially present, but of smaller size than detectable by TEM. A reasonable upper limit estimate for the void density and size can be made using the following assumptions: (1) the total number of interstitials and vacancies as part of extended defects or isolated defects are equal, (2) all of the interstitials are part of dislocation lines, (3) all of the vacancies are part of a spherical void, and (4) the void radius is less than r_v = 1 nm, otherwise they would be visible in TEM, as less than 1 nm bubbles have been reported in UO_2.(65, 66) Based on these assumptions, the concentration of voids n_v should satisfy $4/3\,\pi r_v^3 n_v = \pi b R_d^2 n_d$, where the left and right sides of equation are the calculated number of interstitial and vacancies, respectively. This expression provides an upper limit estimate for n_v (Table I). Adding the void scattering based on these parameters to the stacking fault model for dislocation loops does not significantly alter the estimated conductivity (blue dashed line in Fig. 5b), but improves agreement between model and experiment. Because the contribution of voids fall within the experimental error, we conclude that the contribution of voids can be neglected.

Finally, the potential contribution of point defects to the measured thermal conductivity is considered. Unfortunately, the nature of the point defects can only be speculated and therefore we only make some conclusions based on the estimate for the upper limit of the conductivity reduction. Stimulated by the earlier discussion for the potential source of lattice expansion and knowledge that among all point defects the vacancies have the largest phonon scattering cross-section, we consider oxygen vacancies for this upper limit estimation.(67) First, we use a well-known expression for lattice expansion due to oxygen vacancies $\Delta a/a = 8.52 \times 10^{-2}x$ to estimate the vacancy concentration x in CeO_{2-x} (53). Then, we calculate scattering parameter $\Gamma = xS^2$ using defect scattering cross-section $S^2 = \left(\frac{\Delta M}{\bar{M}}\right)^2$ and vacancy mass mismatch parameter $\frac{\Delta M}{\bar{M}} = -2 - \frac{M_V}{\bar{M}}$.(67) It should be emphasized that the mass mismatch coefficient is notably larger for vacancies compared to other point defects, which typically have a lower value of S^2. This is the primary reason for choosing vacancies for the upper limit estimate of conductivity reduction. The magenta dotted line in Fig. 5(a) represents the upper limit estimate of conductivity reduction due to point defects alone, which is clearly unable to capture experimentally measured trend. Moreover, while the combined influence of dislocation loops (Eq. 6) and point defects (Eq. 2) (represented by the cyan dash-dotted line in Fig.5b) exhibits a reduction in conductivity, the results remain within the experimental error bars. This analysis suggests that point defect alone cannot be responsible for the observed conductivity as the functional form of dose dependency is not captured and more importantly this upper limit estimate is unable to capture the observed reduction. Overall, these results leads us to conclude that point defects like voids are unlikely to play a dominant role in limiting thermal conductivity in these samples.

The analysis presented above is based on single-mode Debye approximation of the phonon dispersion in CeO_2.(68) Detailed representation of the phonon dispersion, even with 3 acoustic branches: one longitudinal and two transverse modes, will have a non-negligible impact on the modeling results. This is attributed to a tendency of different methods used to represent phonon

dispersions to change the relative contribution of phonons with different mean free path (mfp) to thermal conductivity. Dispersions with a heavier weight on short mfp phonons with higher frequencies would predict larger conductivity reduction as defects tend to scatter phonons with short mfp more effectively.(1, 39)

Additionally, phonon lifetime measurements using neutron scattering supplemented by first principles calculations in UO_2 suggested that optical modes also contribute to thermal transport in materials with the fluorite crystalline structure.(69) Recent atomic level conductivity calculations have confirmed similar behavior in CeO_2.(63) More accurate analysis using actual phonon dispersion will require reformulation of the phonon defect scattering rates for each phonon mode, but will not significantly change the conclusion of this work.(1)

These results provide a validation for one controversial observation that can be obtained from classical thermal transport models using relaxation time expression summarized by Klemens.(59) Figure 6 shows that in general clustering of point defects into extended defects leads to thermal conductivity recovery. In this plot, several scenarios each corresponding to a different way to arrange displaced atoms in a crystalline lattice are considered. In all the cases, the fraction of displaced atoms is the same, but the way they are arranged and scatter phonons are different. The conventional trend is that point defects lead to the largest reduction (Eq. 2). As these displaced atoms cluster into 3D voids (Eq.3) or 2D perfect loops (Eq. 4) without annihilation, the conductivity is recovered. On the other hand, arranging displaced atoms into a 2D faulted loops (Eq.6) leads to unusual behavior that exhibits further reduction in conductivity. The latter is attributed to the fact that stacking faults provide a much stronger scattering mechanism likely due to the nature of the strain field surrounding them.(70, 71) It should be emphasized that the results presented in Fig. 6 are derived based on expressions previously reported in the literature(59) and current results provide a means to validate the applicability of Eq. 6 to faulted loops. For practical applications, these results have two implications. On the one hand, it suggests that these nanoscale features previously reported to provide radiation resistance are likely to limit the use of these materials in application requiring efficient thermal transport. On the other hand, for applications where a reduction in phonon-mediated conductivity is desired, inclusion of these nanoscale features offers a material that has a good crystalline structure while also providing strong phonon scattering.

Conclusions

An experimental approach to measure thermal conductivity reduction due to extended defects has been presented. By tuning the irradiation conditions the influence of dislocation loops on thermal transport was isolated. The specific radiation regime used in this study involved proton irradiations of CeO2 with 1.6 MeV ion at 700°C. Thermal conductivity of the shallow damage layer was measured using a modulated thermoreflectance approach. Analysis of experimental results using a classical thermal transport model, informed by microstructure information obtained by high resolution transmission electron microscopy, further support our results. The overall approach offers to be a powerful tool to perform single effect studies on the influence irradiation damage on thermal transport.

Acknowledgements

This material is based upon work supported in part by the Center for Thermal Energy Transport under Irradiation and in part by the Center for Materials Science of Nuclear Fuel. Both are Energy Frontier Research Centers funded by the U.S. Department of Energy, Office of Science, Office of Basic Energy Sciences.

References

1. Wang ZJ, Alaniz JE, Jang WY, Garay JE, Dames C. Thermal Conductivity of Nanocrystalline Silicon: Importance of Grain Size and Frequency-Dependent Mean Free Paths. Nano Letters. 2011;11(6):2206-13.

2. Hu Y, Zeng L, Minnich AJ, Dresselhaus MS, Chen G. Spectral mapping of thermal conductivity through nanoscale ballistic transport. Nature Nanotechnology. 2015;10(8):701-6.

3. Cahill DG, Braun PV, Chen G, Clarke DR, Fan SH, Goodson KE, et al. Nanoscale thermal transport. II. 2003-2012. Applied Physics Reviews. 2014;1(1):011305.

4. Khafizov M, Park I-W, Chernatynskiy A, He L, Lin J, Moore JJ, et al. Thermal Conductivity in Nanocrystalline Ceria Thin Films. Journal of the American Ceramic Society. 2014;97(2):562-9.

5. Zinkle SJ, Snead LL. Designing Radiation Resistance in Materials for Fusion Energy. Annual Review of Materials Research. 2014;44(1):241-67.

6. Beyerlein IJ, Caro A, Demkowicz MJ, Mara NA, Misra A, Uberuaga BP. Radiation damage tolerant nanomaterials. Materials Today. 2013;16(11):443-9.

7. Bai XM, Voter AF, Hoagland RG, Nastasi M, Uberuaga BP. Efficient Annealing of Radiation Damage Near Grain Boundaries via Interstitial Emission. Science. 2010;327(5973):1631-4.

8. Zinkle SJ. Radiation-Induced Effects on Microstructure. Comprehensive Nuclear Materials, Vol 1: Basic Aspects of Radiation Effects in Solids/Basic Aspects of Multi-Scale Modeling. 2012:65-98.

9. Miao YB, Aidhy D, Chen WY, Mo K, Oaks A, Wolf D, et al. The evolution mechanism of the dislocation loops in irradiated lanthanum doped cerium oxide. Journal of Nuclear Materials. 2014;445(1-3):209-17.

10. Sickafus KE. Radiation-Induced Effects on Material Properties of Ceramics (Mechanical and Dimensional). Comprehensive Nuclear Materials, Vol 1: Basic Aspects of Radiation Effects in Solids/Basic Aspects of Multi-Scale Modeling. 2012:123-39.

11. Clinard FW, Hurley GF, Hobbs LW. Neutron-Irradiation Damage in MgO, Al_2O_3 and $MgAl_2O_4$ Ceramics. Journal of Nuclear Materials. 1982;108(1-2):655-70.

12. Snead LL, Burchell TD. Thermal conductivity degradation of graphites due to nuetron irradiation at low temperature. Journal of nuclear materials. 1995;224(3):222 - 9.

13. Staicu D, Wiss T, Rondinella VV, Hiernaut JP, Konings RJM, Ronchi C. Impact of auto-irradiation on the thermophysical properties of oxide nuclear reactor fuels. Journal of Nuclear Materials. 2010;397(1-3):8-18.

14. Snead LL, Zinkle SJ, White DP. Thermal conductivity degradation of ceramic materials due to low temperature, low dose neutron irradiation. Journal of Nuclear Materials. 2005;340(2-3):187-202.

15. Akiyoshi M, Takagi I, Yano T, Akasaka N, Tachi Y. Thermal conductivity of ceramics during irradiation. Fusion Engineering and Design. 2006;81(1-7):321-5.

16. Deng B, Chernatynskiy A, Shukla P, Sinnott SB, Phillpot SR. Effects of edge dislocations on thermal transport in UO_2. Journal of Nuclear Materials. 2013;434(1-3):203-9.

17. Liu XY, Cooper MWD, McClellan KJ, Lashley JC, Byler DD, Bell BDC, et al. Molecular Dynamics Simulation of Thermal Transport in UO_2 Containing Uranium, Oxygen, and Fission-product Defects. Physical Review Applied. 2016;6(4):044015.

18. Lee CW, Chernatynskiy A, Shukla P, Stoller RE, Sinnott SB, Phillpot SR. Effect of pores and He bubbles on the thermal transport properties of UO_2 by molecular dynamics simulation. Journal of Nuclear Materials. 2015;456:253-9.

19. White JT, Nelson AT. Thermal conductivity of UO_{2+x} and U_4O_{9-y}. Journal of Nuclear Materials. 2013;443(1-3):342-50.

20. Ohmichi T, Fukushima S, Maeda A, Watanabe H. On the Relation between Lattice-parameter and O/M Ratio for Uranium-dioxide Trivalent Rare-earth-oxide solid-solution. Journal of Nuclear Materials. 1981;102(1-2):40-6.

21. Suzuki K, Kato M, Sunaoshi T, Uno H, Carvajal-Nunez U, Nelson AT, et al. Thermal and mechanical properties of CeO2. Journal of the American Ceramic Society. 2019;102(4):1994-2008.

22. Nelson AT, Rittman DR, White JT, Dunwoody JT, Kato M, McClellan KJ. An Evaluation of the Thermophysical Properties of Stoichiometric CeO_2 in Comparison to UO_2 and PuO_2. Journal of the American Ceramic Society. 2014;97(11):3652-9.

23. Was GS, Averback RS. Radiation Damage Using Ion Beams. Comprehensive Nuclear Materials, Vol 1: Basic Aspects of Radiation Effects in Solids/Basic Aspects of Multi-Scale Modeling. 2012:195-221.

24. Tonks MR, Liu X-Y, Andersson D, Perez D, Chernatynskiy A, Pastore G, et al. Development of a multiscale thermal conductivity model for fission gas in UO_2. Journal of Nuclear Materials. 2016;469:89-98.

25. Khafizov M, Chauhan V, Wang Y, Riyad F, Hang N, Hurley DH. Investigation of thermal transport in composites and ion beam irradiated materials for nuclear energy applications. Journal of Materials Research. 2017;32(1):204-16.

26. Hofmann F, Mason DR, Eliason JK, Maznev AA, Nelson KA, Dudarev SL. Non-Contact Measurement of Thermal Diffusivity in Ion-Implanted Nuclear Materials. Scientific Reports. 2015;5.

27. Cheaito R, Gorham CS, Misra A, Hattar K, Hopkins PE. Thermal conductivity measurements via time-domain thermoreflectance for the characterization of radiation induced damage. Journal of Materials Research. 2015;30(9):1403-12.

28. Hua Z, Fleming A, Ban H. The study of using a multi-layered model to extract thermal property profiles of ion-irradiated materials. International Journal of Heat and Mass Transfer. 2019;131:206-16.

29. Weisensee PB, Feser JP, Cahill DG. Effect of ion irradiation on the thermal conductivity of UO_2 and U_3O_8 epitaxial layers. Journal of Nuclear Materials. 2013;443(1-3):212-7.

30. Chauhan V, Riyad MF, Du XP, Wei CD, Tyburska-Puschel B, Zhao JC, et al. Thermal Conductivity Degradation and Microstructural Damage Characterization in Low-Dose Ion Beam-Irradiated 3C-SiC. Metallurgical and Materials Transactions E-Materials for Energy Systems. 2017;4(2-4):61-9.

31. David L, Gomes S, Carlot G, Roger JP, Fournier D, Valot C, et al. Characterization of thermal conductivity degradation induced by heavy ion irradiation in ceramic materials. Journal of Physics D-Applied Physics. 2008;41(3):035502.

32. Khafizov M, Yablinsky C, Allen TR, Hurley DH. Measurement of thermal conductivity in proton irradiated silicon. Nuclear Instruments & Methods in Physics Research Section B-Beam Interactions with Materials and Atoms. 2014;325:11-4.

33. He L, Yablinsky C, Gupta M, Gan J, Kirk MA, Allen TR. Transmission electron microscopy investigation of krypton bubbles in polycrystalline CeO_2. Nuclear Technology. 2013;182(2):164-9.

34. He L-F, Gupta M, Yablinsky CA, Gan J, Kirk MA, Bai X-M, et al. In situ TEM observation of dislocation evolution in Kr-irradiated UO_2 single crystal. Journal of Nuclear Materials. 2013;443(1-3):71-7.

35. Zinkle SJ, Konings RJM. 1.03 - Radiation-Induced Effects on Microstructure. Oxford: Elsevier; 2012. p. 65-98.

36. Michel A, Sabathier C, Carlot G, Kaitasov O, Bouffard S, Garcia P, et al. An in situ TEM study of the evolution of Xe bubble populations in UO2. Nuclear Instruments & Methods in Physics Research Section B-Beam Interactions with Materials and Atoms. 2012;272:218-21.

37. Riyad MFC, V., Khafizov M. Implementation of a multilayer model for measurement of thermal conductivity in ion beam irradiated samples using a modulated thermoreflectance approach. Journal of Nuclear Materials. 2018;509.

38. Was GS. Fundamentals of radiation materials science : metals and alloys. Berlin ; New York: Springer; 2007. xxii, 827 p. p.

39. Khafizov M, Yablinsky C, Allen TR, Hurley DH. Measurement of thermal conductivity in proton irradiated silicon. Nuclear Instruments and Methods in Physics Research, B2014. p. 11-4.

40. Pakarinen J, He L, Gupta M, Gan J, Nelson A, El-Azab A, et al. 2.6 MeV proton irradiation effects on the surface integrity of depleted UO_2. Nuclear Instruments & Methods in Physics Research Section B-Beam Interactions with Materials and Atoms. 2014;319:100-6.

41. Weber WJ. Alpha-irradiation damage in CeO_2, UO_2 and PuO_2. Radiation Effects and Defects in Solids. 1984;83(1-2):145-56.

42. Stoller RE, Toloczko MB, Was GS, Certain AG, Dwaraknath S, Garner FA. On the use of SRIM for computing radiation damage exposure. Nuclear Instruments & Methods in Physics Research Section B-Beam Interactions with Materials and Atoms. 2013;310:75-80.

43. Khafizov M, Hurley DH. Measurement of thermal transport using time-resolved thermal wave microscopy. Journal of Applied Physics. 2011;110(8):083525.

44. Hurley D, Schley R, Khafizov M, Wendt B. Local measurement of thermal conductivity and diffusivity. Review of Scientific Instruments. 2015;86(12).

45. Kinoshita C, Hayashi K, Kitajima S. Kinetics of Point-defects in electron-irradiated MgO. Nuclear Instruments & Methods in Physics Research Section B-Beam Interactions with Materials and Atoms. 1984;1(2-3):209-18.

46. Yasunaga K, Yasuda K, Matsumura S, Sonoda T. Nucleation and growth of defect clusters in CeO_2 irradiated with electrons. Nuclear Instruments & Methods in Physics Research Section B-Beam Interactions with Materials and Atoms. 2006;250:114-8.

47. Chen W-Y, Wen J, Kirk MA, Miao Y, Ye B, Kleinfeldt BR, et al. Characterization of dislocation loops in CeO_2 irradiated with high energy Krypton and Xenon. Philosophical Magazine. 2013:1-13.

48. Aidhy DS, Wolf D, El-Azab A. Comparison of point-defect clustering in irradiated CeO_2 and UO_2: A unified view from molecular dynamics simulations and experiments. Scripta Materialia. 2011;65(10):867-70.

49. Edmondson PD, Weber WJ, Namavar F, Zhang YW. Lattice distortions and oxygen vacancies produced in Au+-irradiated nanocrystalline cubic zirconia. Scripta Materialia. 2011;65(8):675-8.

50. Pakarinen J, Khafizov M, He L, Wetteland C, Gan J, Nelson AT, et al. Microstructure changes and thermal conductivity reduction in UO_2 following 3.9 MeV He^{2+} ion irradiation. Journal of Nuclear Materials. 2014;454(1-3):283-9.

51. Willis JR, Bitllough R, Stoneham AM. The effect of dislocation loops on the lattice parameter, determined by X-ray diffraction. Philosophical Magazine A. 1983;48(1):95-107.

52. Larson BC. High-precision Measurements of Lattice-parameter Changes in Neutron-irradiated Copper. Journal of Applied Physics. 1974;45(2):514-8.

53. Mogensen M, Sammes NM, Tompsett GA. Physical, chemical and electrochemical properties of pure and doped ceria. Solid State Ionics. 2000;129(1-4):63-94.

54. Pakarinen J, He LF, Hassan AR, Wang YQ, Gupta M, El-Azab A, et al. Annealing-induced lattice recovery in room-temperature xenon irradiated CeO_2: X-ray diffraction and electron energy loss spectroscopy experiments. Journal of Materials Research. 2015;30(9):1555-62.

55. Palomares RI, Tracy CL, Zhang FX, Park C, Popov D, Trautmann C, et al. In situ defect annealing of swift heavy ion irradiated CeO_2 and ThO_2 using synchrotron X-ray diffraction and a hydrothermal diamond anvil cell. Journal of Applied Crystallography. 2015;48:711-7.

56. Wang YZ, Hurley DH, Luther EP, Beaux MF, Vodnik DR, Peterson RJ, et al. Characterization of ultralow thermal conductivity in anisotropic pyrolytic carbon coating for thermal management applications. Carbon. 2018;129:476-85.

57. Klemens PG. Theory of thermal conduction in dielectric solids: effect of radiation damage. Nuclear Instruments & Methods in Physics Research Section B-Beam Interactions with Materials and Atoms. 1984;1(2-3):204-8.

58. Callaway J. Model for lattice thermal conductivity at low temperatures. Physical Review. 1959;113(4):1046-51.

59. Klemens PG. Thermal conductivity and lattice vibration modes. Solid State Physics-Advances in Research and Applications. 1958;7:1-98.

60. Wang Y, Hurley DH, Hua Z, Sha G, Raetz S, Gusev VE, et al. Nondestructive characterization of polycrystalline 3D microstructure with time-domain Brillouin scattering. Scripta Materialia. 2019;166:34-8.

61. Morelli DT, Perry TA, Farmer JW. Phonon-scattering in lightly neutron-irrdiated diamond. Physical Review B. 1993;47(1):131-9.

62. Turk LA, Klemens PG. Phonon scattering by impurity platelet precipitates in diamond. Physical Review B. 1974;9(10):4422-8.

63. Malakkal L, Prasad A, Oladimeji D, Jossou E, Ranasinghe J, Szpunar B, et al. Atomistic and experimental study on thermal conductivity of bulk and porous cerium dioxide. Scientific Reports. 2019;9(1):6326.

64. Wang T, Carrete J, van Roekeghem A, Mingo N, Madsen GKH. Ab initio phonon scattering by dislocations. Physical Review B. 2017;95(24).

65. He L, Valderrama B, Hassan AR, Yu J, Gupta M, Pakarinen J, et al. Bubble formation and Kr distribution in Kr-irradiated UO2. Journal of Nuclear Materials. 2015;456:125-32.

66. Sabathier C, Martin G, Michel A, Carlot G, Maillard S, Bachelet C, et al. In-situ TEM observation of nano-void formation in UO_2 under irradiation. Nuclear Instruments & Methods in Physics Research Section B-Beam Interactions with Materials and Atoms. 2014;326:247-50.

67. Klemens PG. Phonon scattering by oxygen vacancies in ceramics. Physica B. 1999;263:102-4.

68. Clausen K, Hayes W, Macdonald JE, Osborn R, Schnabel PG, Hutchings MT, et al. Inelastic Neutron-Scattering Investigation of the Lattice Dynamics of ThO_2 and CeO_2. Journal of the Chemical Society-Faraday Transactions Ii. 1987;83:1109-12.

69. Pang JWL, Buyers WJL, Chernatynskiy A, Lumsden MD, Larson BC, Phillpot SR. Phonon Lifetime Investigation of Anharmonicity and Thermal Conductivity of UO_2 by Neutron Scattering and Theory. Physical Review Letters. 2013;110(15):5.

70. Klemens PG. The scattering of low-frequency lattice waves by static imperfections. Proceedings of the Physical Society of London Section A. 1955;68(12):1113-28.

71. Klemens PG. Some scattering problems in conduction theory. Canadian Journal of Physics. 1957;35(4):441-50.

Figure Captions

Figure 1. TEM microstructure characterization revealing dislocation loops in proton irradiated CeO_2: (a) 0.2 dpa sample and (b) 1.0 dpa sample.

Figure 2. Determination of loop orientation: (a) High-resolution observation from the edge-on loops. Fourier transforms from the regions surrounded by white boxes in (b) and (c) indicate that the loops lay on the (111) planes.

Figure 3. X-ray diffraction patterns of (311) peak in irradiated and as received CeO_2 samples.

Figure 4. Thermal transport measurements in proton irradiated CeO_2. (a) Thermal wave profiles measured at 10 kHz. (b) Impact of thermal wave penetration depth on measured effective diffusivity.

Figure 5. Analysis of conductivity reduction in proton irradiated samples using different models capturing the impact of dislocation loops and potential contribution of point defects and voids. (a) Single defect contribution and (b) impact of multiple defects.

Figure 6. Impact of irradiation induced defects on conductivity reduction.

Table I. Characterization summary

	as-received	0.2dpa	1.0 dpa
Dislocation loop radius, R_d (nm)	-	3.7 ± 1.1	7.4 ± 2.0
Dislocation loop density, n_d (10^{21} m^{-3})	-	3.9 ± 0.2	6.1. ± 1.2
Thermal conductivity, κ (W/mK)	19.7±1.3	17.5±1.6	12.0±1.3
Measured lattice expansion, Δa/a	-	3.3×10^{-4}	4.1×10^{-4}
Estimated lattice expansion due to loops	-	0.16×10^{-4}	0.95×10^{-4}
Estimated oxygen vacancy concentration (per U atom)		3.9×10^{-3}	4.8×10^{-3}
Estimated void concentration (10^{22} m^{-3})	-	1.1	6.8

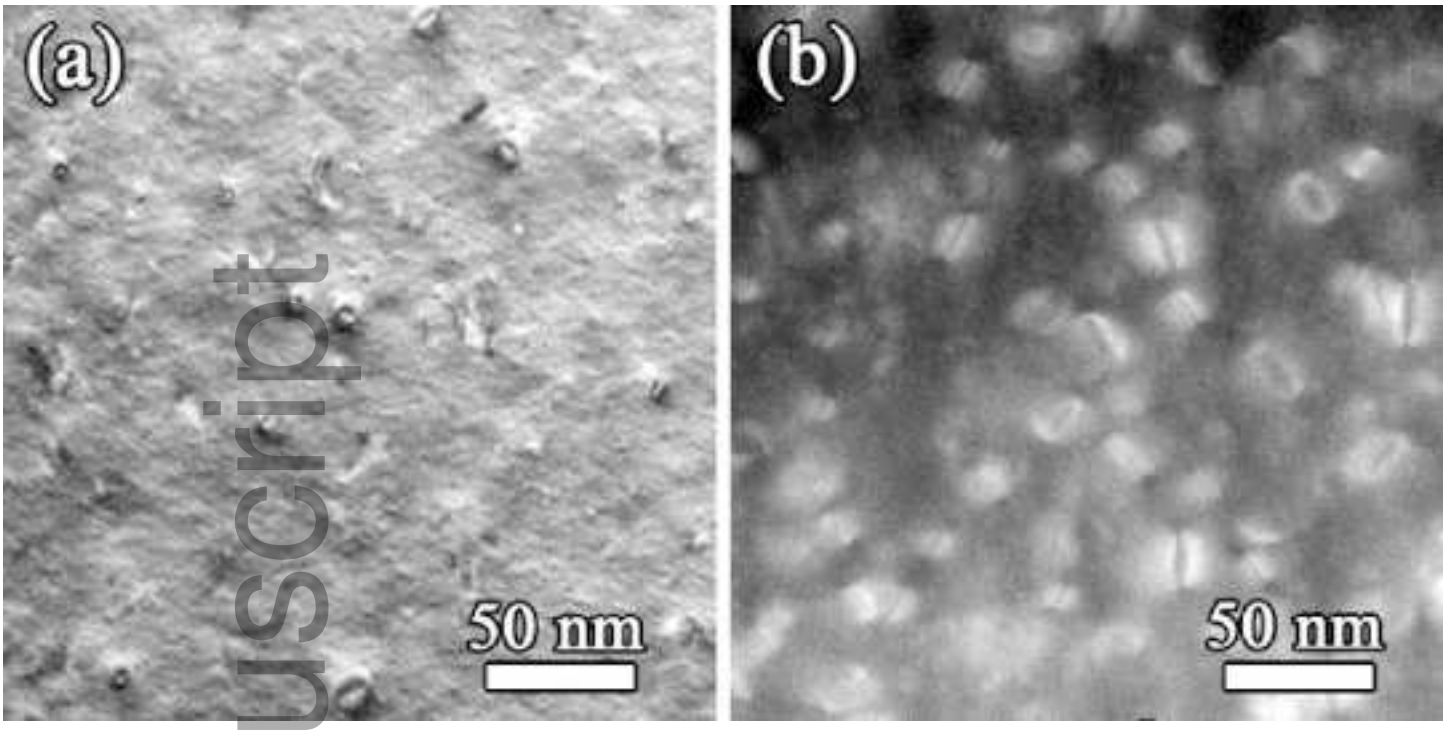

jace_16616_f1.tiff

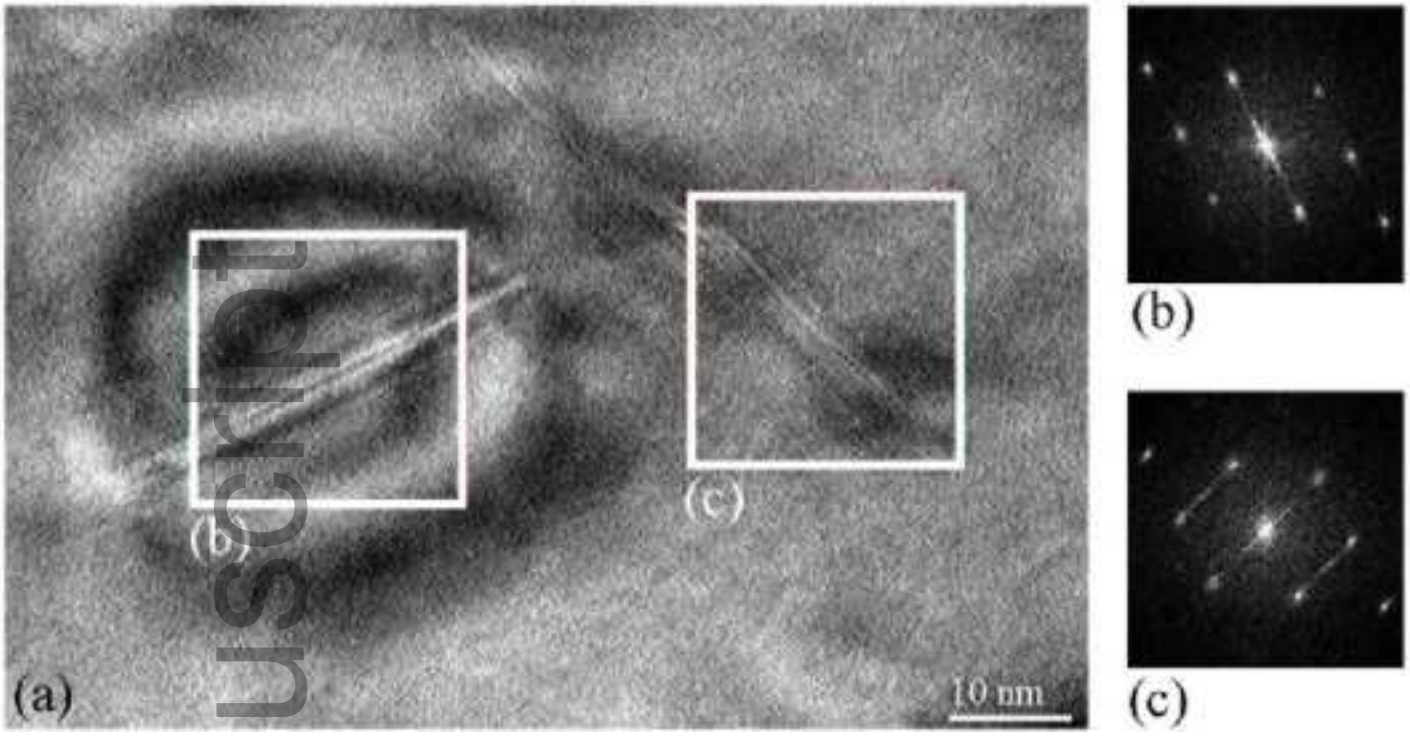

jace_16616_f2.tiff

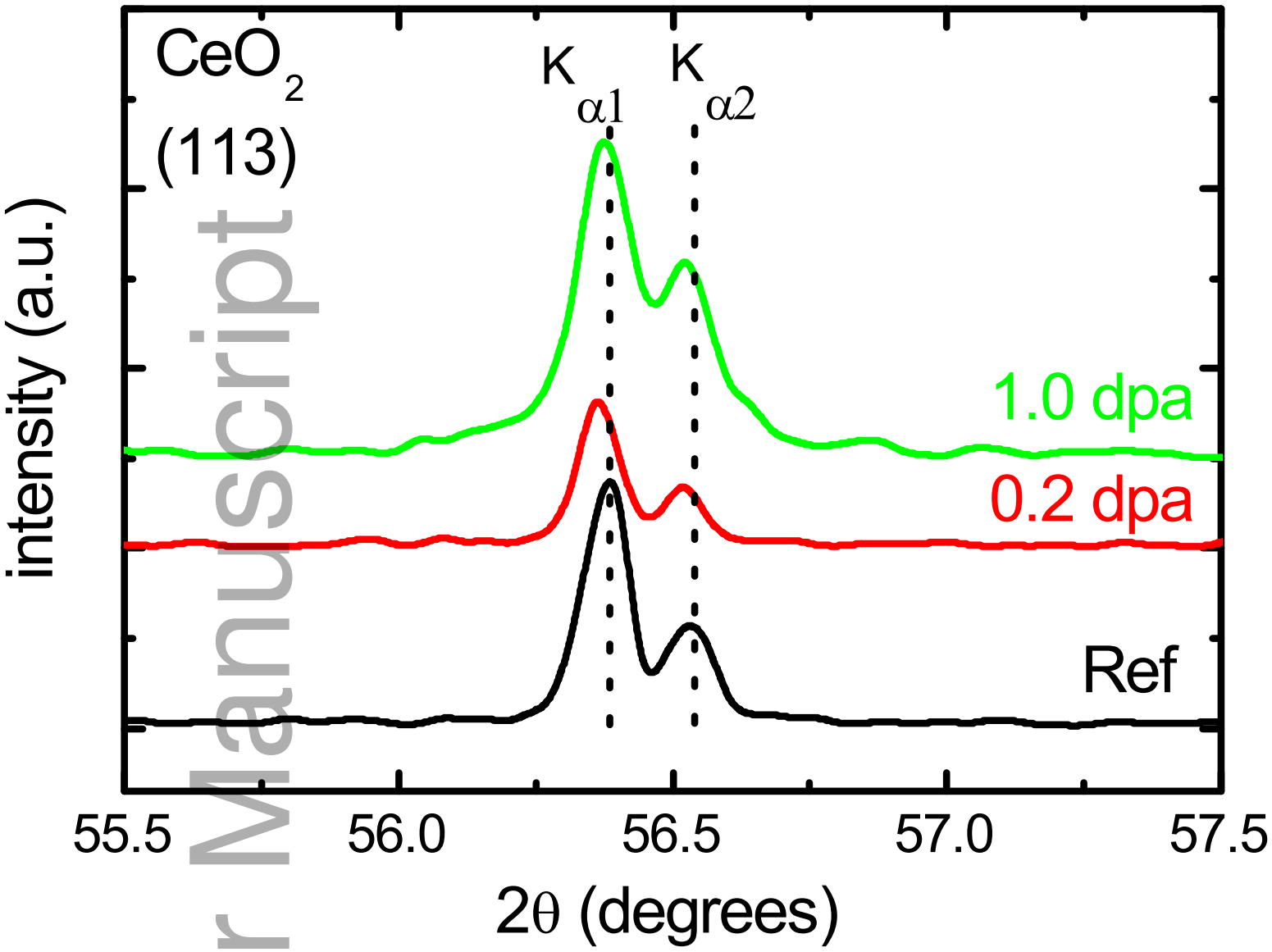

jace_16616_f3.eps

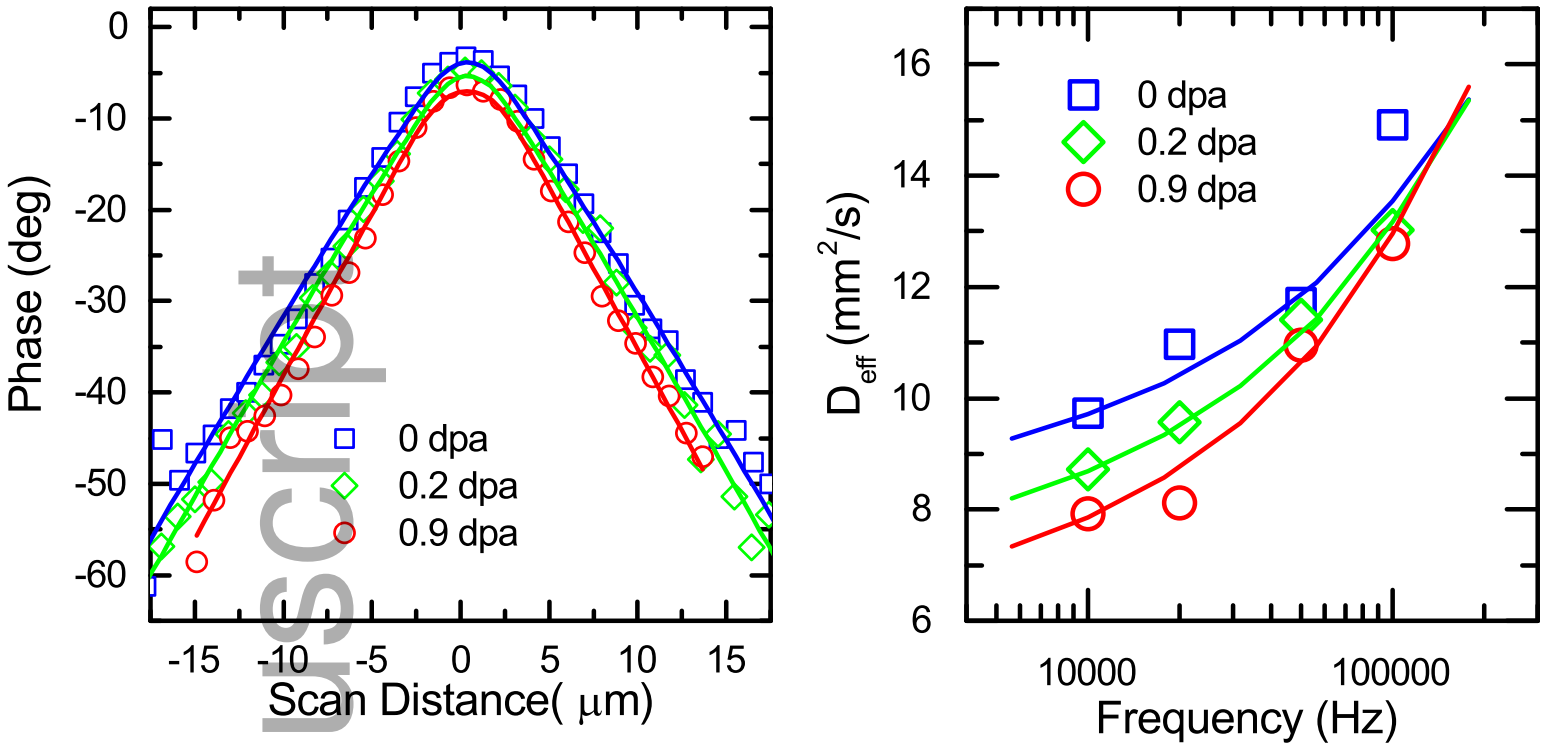

jace_16616_f4.eps

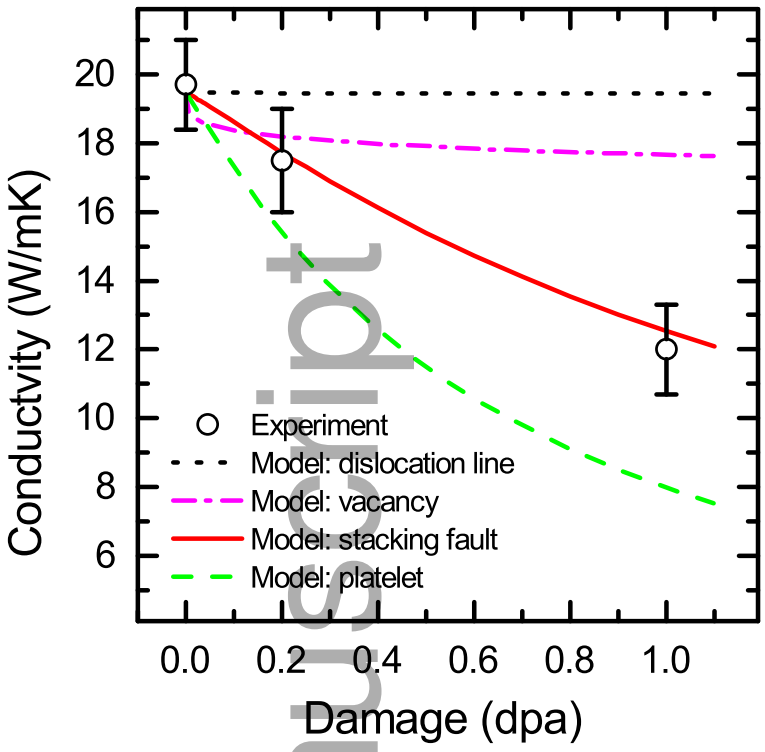

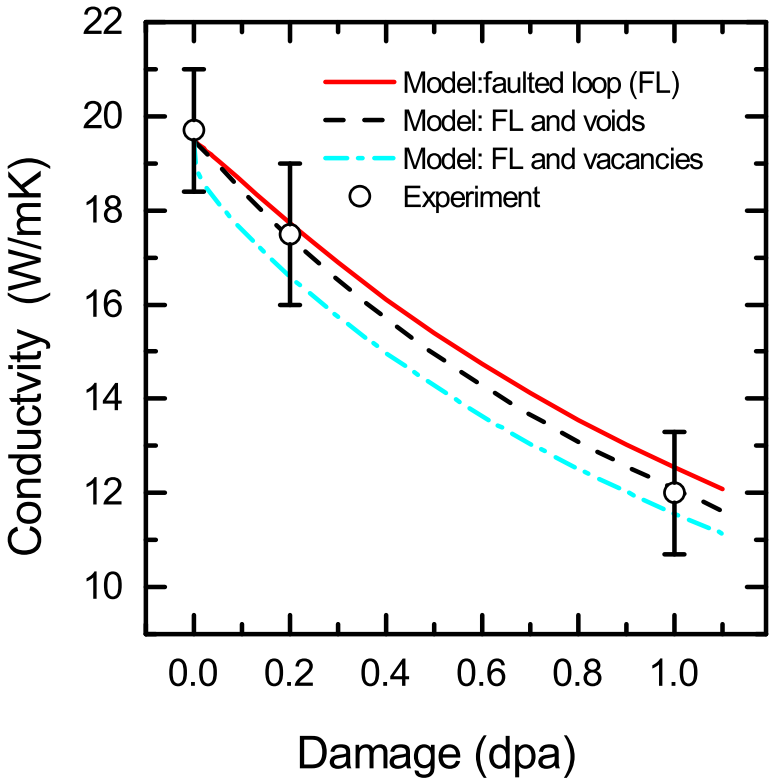

jace_16616_f5.eps

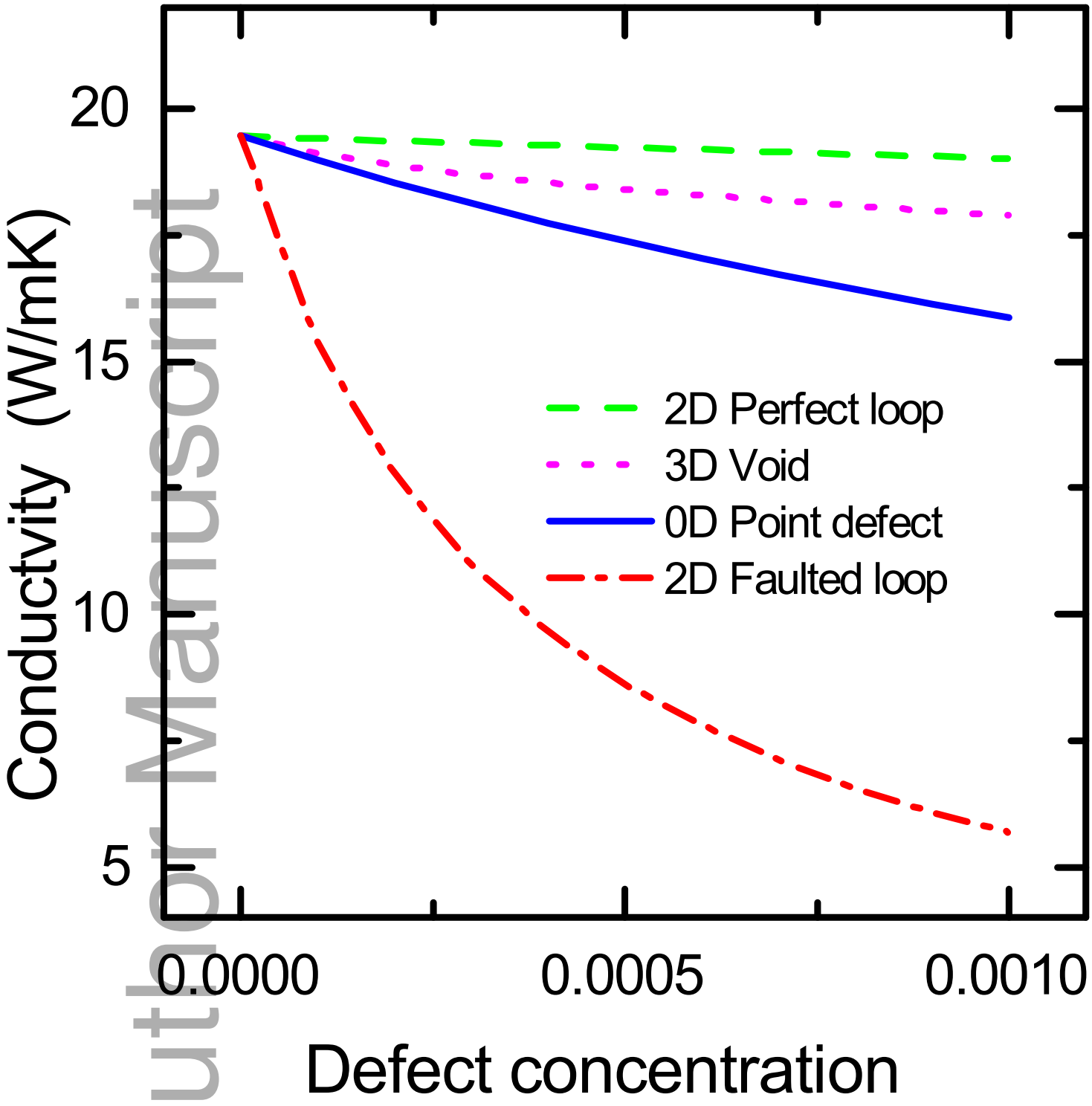

jace_16616_f6.eps